

Polypeptide Folding-Mediated Tuning of the Optical and Structural Properties of Gold Nanoparticle Assemblies

Daniel Aili,^{†,‡,||} Piotr Gryko,^{†,‡} Borja Sepulveda,[⊥] John A. G. Dick,^{†,‡} Nigel Kirby,[¶] Richard Heenan,[#] Lars Baltzer,[▽] Bo Liedberg,^{||,○} Mary P. Ryan,^{†,*} and Molly M. Stevens^{*,†,‡,§}

[†]Department of Materials, [‡]Institute for Biomedical Engineering, [§]Department of Bioengineering, Imperial College London, Exhibition Road, SW7 2AZ London, United Kingdom

^{||}Centre for Biomimetic Sensor Science, School of Materials Science and Engineering, Nanyang Technological University, Research Techno Plaza, Sixth Storey XFrontiers Block, 50 Nanyang Avenue, 637553 Singapore

[⊥]Research Center on Nanoscience and Nanotechnology (CIN2) CSIC, Campus UAB Edificio Q third floor, 08193 Bellaterra, Barcelona, Spain

[¶]Australian Synchrotron, Clayton, Victoria 3168, Australia

[#]ISIS, Rutherford Appleton Laboratory, Oxfordshire, United Kingdom

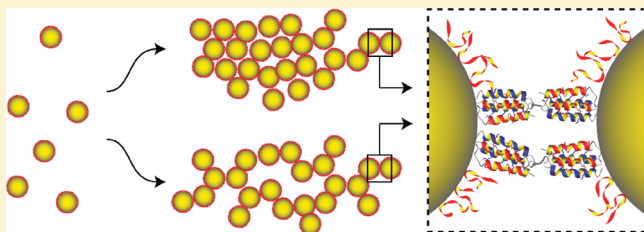
[▽]Department of Biochemistry and Organic Chemistry, Uppsala University, BMC, Box 576, 751 23 Uppsala, Sweden

[○]Division of Molecular Physics, Department of Physics, Chemistry and Biology, Linköping University, 581 83 Linköping, Sweden

S Supporting Information

ABSTRACT: Responsive hybrid nanomaterials with well-defined properties are of significant interest for the development of biosensors with additional applications in tissue engineering and drug delivery. Here, we present a detailed characterization using UV–vis spectroscopy and small angle X-ray scattering of a hybrid material comprised of polypeptide-decorated gold nanoparticles with highly controllable assembly properties. The assembly is triggered by a folding-dependent bridging of the particles mediated by the heteroassociation of immobilized helix–loop–helix polypeptides and a complementary nonlinear polypeptide present in solution. The polypeptides are de novo designed to associate and fold into a heterotrimeric complex comprised of two disulfide-linked four-helix bundles. The particles form structured assemblies with a highly defined interparticle gap (4.8 ± 0.4 nm) that correlates to the size of the folded polypeptides. Transitions in particle aggregation dynamics, mass-fractal dimensions and ordering, as a function of particle size and the concentration of the bridging polypeptide, are observed; these have significant effects on the optical properties of the assemblies. The assembly and ordering of the particles are highly complex processes that are affected by a large number of variables including the number of polypeptides bridging the particles and the particle mobility within the aggregates. A fundamental understanding of these processes is of paramount interest for the development of novel hybrid nanomaterials with tunable structural and optical properties and for the optimization of nanoparticle-based colorimetric biodetection strategies.

KEYWORDS: Gold nanoparticles, polypeptides, folding, helix–loop–helix, small angle X-ray scattering (SAXS)



Self-assembly has emerged as a promising route for fabrication of nanomaterials with novel properties suitable for applications in tissue engineering,^{1–3} therapeutics,⁴ drug delivery,⁵ and biosensing.^{6,7} A key issue in the design of materials that are chemically and structurally defined at the nanoscale is the requirement of reproducible methods for precisely controlling the assembly process and the spatial arrangement of the components. A promising route to guide the assembly of nanosized inorganic building blocks is through the use of biological or biomimetic macromolecules such as DNA,^{8,9} proteins,¹⁰ and polypeptides.^{11,12} Biomolecules provide chemical and structural flexibility along with highly controllable and programmable intermolecular interactions. This has enabled the specific, controlled, and reversible assembly of a plethora of different

inorganic nanomaterials, including gold nanoparticles (Au NPs). The presence of order in nanoscale assemblies often relies on very homogeneous and monodisperse particles along with strong interaction potentials. However, soft interaction potentials typically found in biological and biomimetic systems, where the interaction energy is on the order of thermal energy, still allow for spontaneous order formation despite certain defects and polydispersity of the constituent elements.¹³ The utilization of biomolecules to guide the assembly of inorganic nanoscale building

Received: October 10, 2011

Revised: October 31, 2011

Published: November 02, 2011

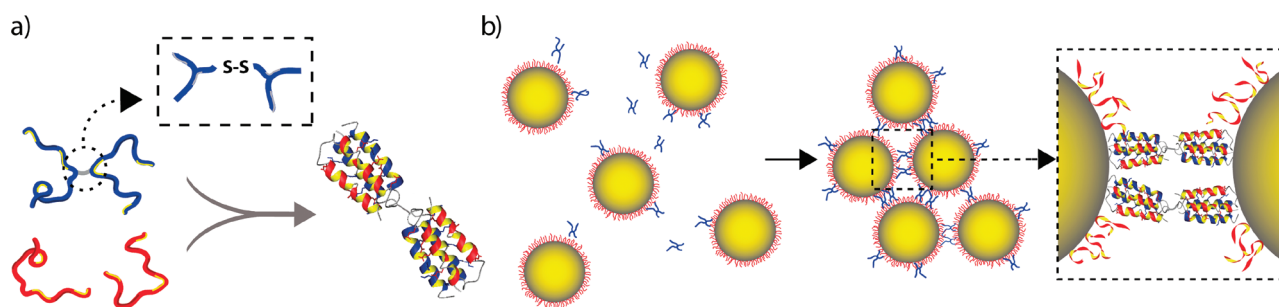


Figure 1. (a) Schematic illustration of the formation of the heterotrimeric complex formed as a result of the heteroassociation between the lysine-rich, nonlinear, 84 residue polypeptide JR2KC₂ and two complementary glutamate-rich helix–loop–helix polypeptides (JR2EC). JR2KC₂ and JR2EC are shown in blue and red, respectively. The peptides fold into two disulfide-linked four-helix bundles upon association. (b) Addition of JR2KC₂ to Au NPs modified with JR2EC induces a rapid and folding dependent bridging aggregation of the particles.

blocks thus presents a powerful approach to control the assembly and introduce order at the nanoscale in hybrid materials.

Au NPs are of particular interest in hybrid materials because of their optical properties that enable a convenient transduction mechanism for biosensor applications, based on the difference in color of dispersed and aggregated particles. DNA and polypeptide-modified Au NPs have consequently been widely utilized for colorimetric detection of a broad range of analytes,¹⁴ including metal ions,¹⁵ nucleotides,¹⁶ and proteins.^{17–19} The distinct color of Au NPs is the result of collective electron oscillations, known as localized surface plasmon resonance (LSPR). The LSPR gives rise to a pronounced extinction band in the visible wavelength spectrum, and the position and width of the LSPR band are highly affected by particle aggregation. Particle aggregation results in a spectral red shift and broadening of the peak. The magnitude of this shift depends primarily on particle size, aggregate density, fractal dimensions, and aggregate size,^{20,21} whereas the rate of change of the spectral shift depends on aggregate size and growth rate. Information on the aggregate structure can be utilized to better understand and tune the optical properties of Au NP assemblies but can also be compared to common colloidal aggregate growth models,^{22,23} such as diffusion-limited colloid aggregation (DLCA), reaction-limited colloid aggregation (RLCA), and compact cluster (CC) formation, in order to better understand the interactions involved in the assembly process.

We have previously described a strategy for controlled and reversible assembly of Au NPs based on a folding-dependent bridging using de novo designed polypeptides as schematically described in Figure 1.²⁴ We have also recently employed this material in an assay for robust colorimetric detection of phospholipase activity.¹⁷ Here we present an in depth investigation of the optical and structural properties of this hybrid nanomaterial using small angle X-ray scattering (SAXS) combined with UV–vis spectroscopy that provides a better understanding of the assembly process and information on how to tune and control these properties by employing highly specific biomolecular interactions.

The polypeptide that was immobilized on the Au NPs is a glutamic acid-rich 42 amino acid helix loop-helix polypeptide (JR2EC). JR2EC have no ordered secondary structure at neutral pH but homodimerize and fold into a four-helix bundle at slightly acidic pH or in the presence of a range of divalent cations.^{25,26} A cysteine residue was included in the loop region to facilitate directed immobilization on Au NPs. In solution, two JR2EC monomers can heteroassociate with a second polypeptide

(JR2KC₂) and fold into two disulfide-linked four-helix bundles as schematically illustrated in Figure 1a.²⁴ JR2KC₂ is a nonlinear 84 amino acid polypeptide rich in lysine residues, designed as two separate helix–loop–helix polypeptides (JR2KC) that are covalently linked by a disulfide bridge between cysteine residues located in the loop. Au NPs functionalized with JR2EC aggregate extensively and rapidly in the presence of JR2KC₂.²⁴ The assembly is mainly driven by the heteroassociation and folding of the polypeptides (Figure 1b). The influence of folding on the assembly of the particles was determined using a polypeptide with the identical amino acid sequence to JR2EC but all L-Ala were replaced by D-Ala, which effectively prevented this peptide from folding. This system thus offers an interesting and useful possibility to assemble nanoparticles by employing highly specific molecular interactions.

In this work, we confirm that the particles form regularly ordered aggregates with well-defined particle spacing corresponding to the size of the folded four-helix bundles. There is also an intricate relationship between the dynamics, density and internal structure of the aggregates and hence their optical properties with the size of the Au NPs and the concentration of JR2KC₂. These observations enable strategies for tuning of the morphology and the optical properties of gold nanoparticle assemblies, which can have a profound impact on their performance in colorimetric sensors and on the design of hybrid materials with a controllable spatial ordering at the nanoscale. This work is also of large interest for the fundamental understanding of the assembly processes of peptide-based nanomaterials and highlights a number of aspects that have a large influence on the dynamics and organization of nanoparticle assemblies.

Results and Discussion. The 42-amino acid helix–loop–helix polypeptide JR2EC was immobilized on Au NPs with diameters of 10, 20, and 40 nm via a thiol residue in the loop region. The actual sizes of the as-received Au NPs were found to be 9.4 ± 0.8 , 18.3 ± 2 , and 37.8 ± 4 nm using SAXS, which correlated closely to the sizes obtained by transmission electron microscopy (TEM), 9.3 ± 0.7 , 18.9 ± 1 , and 38.4 ± 3 nm. The JR2EC polypeptides were immobilized under conditions yielding a relatively low surface coverage ($\sim 60\%$ of a monolayer) in order to facilitate the heteroassociation but also to minimize the influence of particle curvature on the surface concentration.²⁷ The heteroassociation of JR2KC₂ to the immobilized polypeptides was confirmed and characterized on planar gold surfaces using surface plasmon resonance (SPR), Figure 2. SPR was utilized to obtain the dissociation constant ($K_D = 0.3 \mu\text{M}$) for the heteroassociation of JR2KC₂ to JR2EC immobilized on gold.

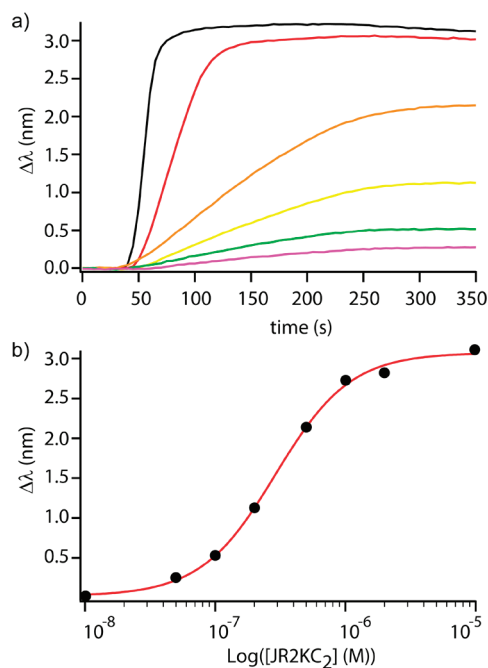


Figure 2. (a) SPR response for the heteroassociation of JR2KC₂ to JR2EC immobilized on gold surfaces, (black) 10 μ M, (red) 1 μ M, (orange) 0.5 μ M, (yellow) 0.2 μ M, (green) 0.1 μ M, (purple) 50 nM. (b) Equilibrium response versus concentration. The solid line represents the theoretical fit for the equilibrium response as function of JR2KC₂ concentration with the dissociation constant $K_d = 0.3 \mu\text{M}$, based on a bimolecular dissociation model.

This K_D value is interestingly significantly lower than for the dimerization of the corresponding monomers in solution ($K_D = 0.02 \text{ mM}$),²⁷ which could be due to the strong electrostatic interactions between the highly negatively charged surface and the positively charged JR2KC₂ resulting in a pronounced pre-concentration effect.

When investigating the heteroassociation-mediated bridging of the gold nanoparticles, the absolute concentrations of the polypeptides were assumed to be more critical than the concentrations of nanoparticles. In order to keep the concentration of JR2EC constant in all samples and for all particle sizes, the concentrations of particles were thus adjusted with respect to surface area. In all measurements, the concentrations of particles were 1.6, 0.4, and 0.09 nM for 10, 20, and 40 nm Au NPs respectively, corresponding to a particle surface area per volume of suspension of $0.3 \text{ m}^2 \text{ L}^{-1}$, giving a concentration of immobilized JR2EC of approximately 70 nM. The concentration of unbound peptides was reduced to less than 0.1 nM by repeated centrifugations and exchange of buffer.

The position of the LSPR band (λ_{max}) of the dispersed particles was similar for all three sizes of particles in the size range used here (10–40 nm), showing maxima at 523–528 nm after peptide functionalization. Particle aggregation, induced by addition of JR2KC₂, resulted in immediate and pronounced spectral changes including a red shift and broadening of the LSPR band with the optical shift varying significantly with particle size for the same concentration of JR2KC₂. Representative UV–vis spectra, before and after addition of 0.1 μ M of JR2KC₂, are shown in Figure 3. The 10 nm particles displayed homogeneously red-shifted spectra, approximately 35 nm after about 20 min, and

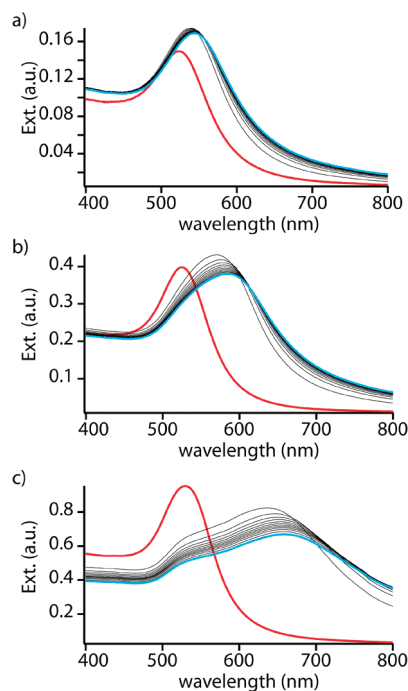


Figure 3. UV–vis spectra of the JR2EC decorated Au NPs with radii of (a) 10 (b) 20, and (c) 40 nm before and after addition of 0.1 μ M of JR2KC₂. Spectra were recorded with 2 min intervals for 30 min. JR2KC₂ was added after 6 min which resulted in a significant red shift and broadening of the LSPR band. Spectra before addition of JR2KC₂ are shown in red and the last recorded spectrum for each particle size is shown in blue.

a slight broadening of the LSPR band accompanied by an increase in extinction. The changes in the spectra of the 20 nm particles were more pronounced, demonstrating a larger red shift ($\sim 50 \text{ nm}$) and a significant broadening. The spectra of the 40 nm particles were further red shifted ($\sim 120 \text{ nm}$) while having a broad shoulder remaining at the original LSPR peak position. The shift in the position of the LSPR extinction maximum ($\Delta\lambda_{\text{max}}$) gives a good description of the optical spectral changes during the aggregation process but does not reveal any information about peak broadening. The changes in the ratio of the integrals from 700 to 550 nm and 540 to 490 nm, the so-called $\Delta A/D$ ratio, can be used as a highly sensitive and accurate method to also describe these spectral changes (Supporting Information Figure S1).²⁸

$\Delta A/D$ and $\Delta\lambda_{\text{max}}$ as a function of JR2KC₂ concentration and time for the different sizes of Au NPs are presented in Figure 4. The corresponding full UV–vis spectra are included in the Supporting Information (Figures S2–S4). The measurements were conducted before and directly after introducing JR2KC₂ into the samples and spectra were subsequently recorded every two minutes for 30 min. The onset of aggregation was very rapid ($< 1 \text{ min}$) for all sizes of particles for concentrations of JR2KC₂ spanning over 3 orders of magnitude, but distinct variations in $\Delta A/D$, $\Delta\lambda_{\text{max}}$ and aggregation rate were observed for different particle sizes. The 10 nm particles showed no, or only very small, spectral changes for the two highest (25 and 10 μ M), and the two lowest concentrations (25 and 5 nM) whereas the 20 and 40 nm particles aggregated at all except the lowest concentration, producing extensive spectral red shifts. For 10 nm Au NPs aggregation occurred rapidly for 0.1 μ M and 0.5 μ M JR2KC₂

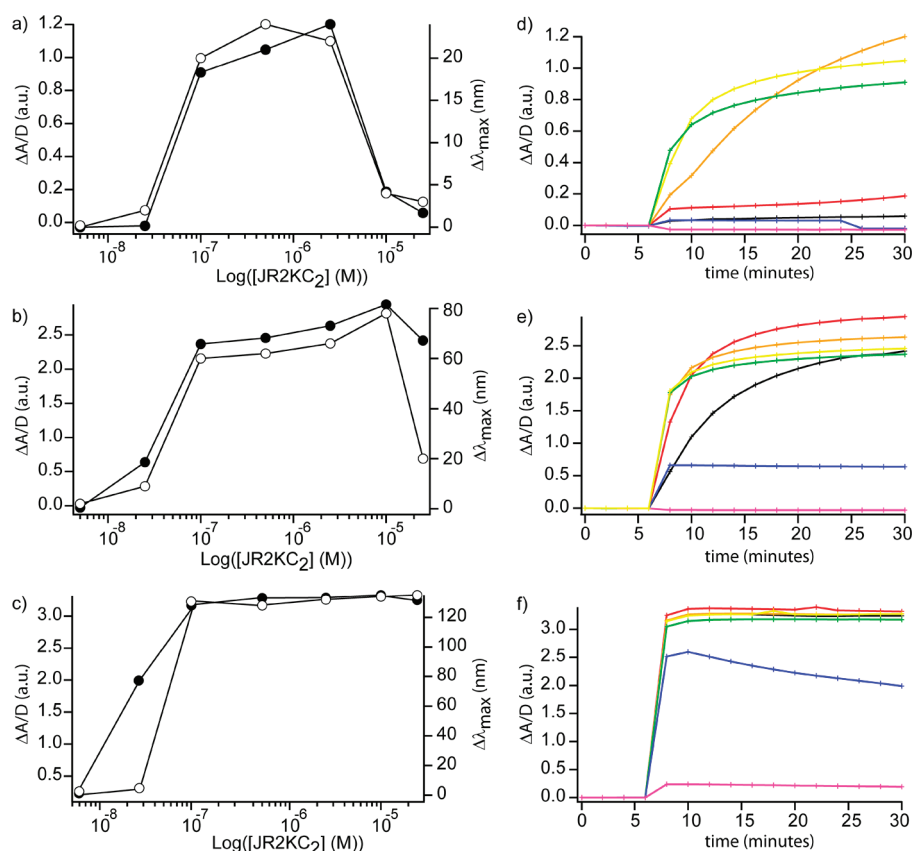


Figure 4. (a–c) $\Delta A/D$ and $\Delta \lambda_{\text{max}}$ as a function of JR2KC₂ concentration and (d–f) change in $\Delta A/D$ over time for 10 nm (a,d), 20 nm (b,e), and 40 nm (c,f) Au NPs. In (a–c), data were obtained 25 min after addition of JR2KC₂. (●) $\Delta A/D$ ratio and (○) $\Delta \lambda_{\text{max}}$. In (d–f), JR2KC₂ was added after 6 min and spectra recorded with 2 min interval for 30 min. The concentration of JR2KC₂ was (black) 25 μM , (red) 10 μM , (orange) 2.5 μM , (yellow) 0.5 μM , (green) 0.1 μM , (blue) 25 nM, and (purple) 5 nM.

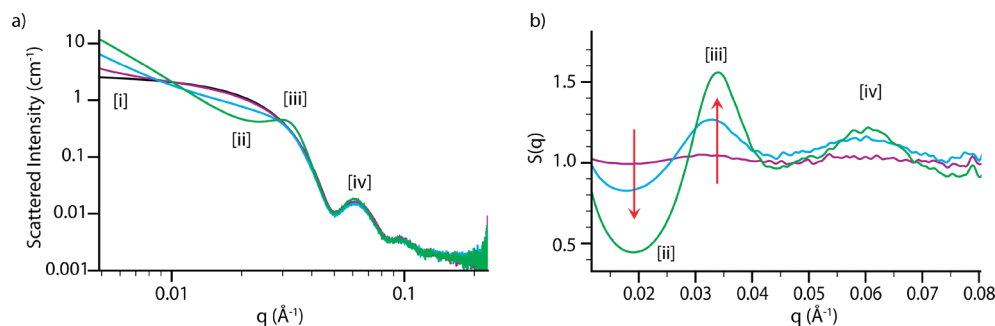


Figure 5. (a) Scattered intensity of 20 nm Au NPs with increasing JR2KC₂ concentrations and (b) the calculated structure factor $S(q)$ describing interparticle correlations. Concentrations of JR2KC₂ are (black) 0 nM, (purple) 5 nM, (blue) 25 nM, (green) 0.1 μM . In (a), the onset of aggregation gave rise to logarithmic scattering at low q [i]. From intermediate to high q , a decrease in scattering [ii] was observed as well as a structural peak at [iii] and small shifts at high q [iv]. In (b) the regions [ii] to [iii] were fitted using a sticky hard sphere model and [iii] to [iv] with a para-crystalline approximation. Note, that regions [ii] to [iv] in (a) are mapped directly onto [ii] to [iv] in (b). The arrows in (b) indicate the change in $S(q)$ with increasing JR2KC₂ concentration.

and more slowly in the presence of 2.5 μM JR2KC₂. For 20 nm Au NPs, the rate of change in the optical shift decreased at the two highest concentrations of JR2KC₂. The slower aggregation rate observed for the 20 nm particles and absence of aggregation for the 10 nm particles at higher JR2KC₂ concentrations is attributed to a charge reversal of particles from slightly negative to highly positive when a large amount of the bridging polypeptide is bound, which improves the electrostatic stability of

particles. There is also a saturation of available binding sites that reduces the probability of bridging.

In situ SAXS was employed in order to correlate the optical properties with the structural properties of the assemblies at different concentrations of polypeptides and particles sizes. The complete set of SAXS scattering profiles are presented in Figures S5–S7 in the Supporting Information. Figure 5 illustrates the SAXS scattering intensities of the 20 nm Au NPs with increasing

JR2KC₂ concentrations from 0 to 0.1 μM 15 min after introducing the bridging polypeptide. The scattered intensity $I(q)$ from a collection of particles can be described in terms of the particle form factor $P(q)$,^{29–31} and the system structure factor $S(q)$, according to eq 1

$$I(q) = nv^2\Delta\rho^2P(q)S(q) \quad (1)$$

where $\Delta\rho$ is the difference in electron density between the particles and solvent, n is the scattering particle concentration (particles/cm³) and v the volume of scattering particles (in cm³). The form factor $P(q)$ describes the ensemble averaged shape of scattering objects in solution whereas the structure factor $S(q)$ accounts for the interference introduced by interparticle correlations. For a dilute noninteracting system of scatterers, $S(q)$ has a value of unity.^{29–31} Dispersed Au NPs were fitted using a spherical form factor assuming a log-normal particle size distribution as described and illustrated in the Supporting Information (Figure S8). In agreement with UV–vis data, an increase in aggregation was observed as the concentration of the bridging polypeptide was increased to 0.1 μM . The onset of aggregation gave rise to characteristic logarithmic scattering at low q [i] in Figure 5a),³² which provides a measure of the fractal dimension of the aggregates formed (Supporting Information S9, S10). From intermediate to high q , destructive interference [ii] was obtained and the structural peak at [iii] and small deviations at high q [iv] appeared. This region, mid to high q [ii to iv], provides information on short-range interparticle correlations, with characteristic features visible across all three particle sizes (Figure S5–S7, Supporting Information). A clearer picture of short-range interparticle correlations can be obtained by removing the scattering contribution from individual particles, to yield the structure factor $S(q)$ which is purely determined by interparticle correlations (Figure 5b). Note that in Figure 5b the Roman numerals are kept consistent, that is, regions [ii] to [iv] in Figure 5a are mapped directly onto [ii] to [iv] in Figure 5b. The regions [ii] to [iii] in Figure 5b and in the corresponding data sets of the 10 and 40 nm particles (Figures S11–S13, Supporting Information) were fitted using a sticky hard sphere model (the Baxter model).^{33–36} The Baxter model is defined by an attractive thin square well potential, which means that once adjacent particles reach within a hard sphere radius (r_{hs}) an infinite repulsive potential is introduced to model the repulsion induced by the overlap of the immobilized polypeptides. More information on the Baxter model is included in the Supporting Information and in Figure S13 (Supporting Information). This model allows for an estimate of particle r_{hs} , aggregate volume fraction (ϕ) and particle stickiness (τ). The r_{hs} describes the radial distance from the center of the particle to the point at which particles begin to repel each other. In this context, r_{hs} is assumed to describe the radius of the combined particle and peptide. The τ is a dimensionless quasi-temperature³⁷ with the reciprocal $1/\tau$ providing an estimate of the adhesive potential between particles. However, the ϕ and τ are not completely independent^{35,36,38–40} as an increase in attractive potential can be partially compensated by a decrease in the aggregate volume.^{37,38,40–42} This makes it difficult to find a unique independent solution for both τ and ϕ .⁴¹ To simplify the fitting process τ was set to a fixed value and under least-squares free fitting, τ was found to vary $\tau = 0.1 \pm 0.02$. Hence τ was set to 0.1. Under these conditions, ϕ and r_{hs} were fitted to yield a unique result. An increase in ϕ hence describes both a positive change in volume fraction and particle interaction potential.

The high q regions (Figure 5 [iii] to [iv]) demonstrate a primary peak (q_0) and a weak secondary peak (q_n) with a position ratio (q_0/q_n) of 1:1.73, indicating the presence of semicrystallinity within the system. Fitting the relative positions (i.e., ratios) of these peaks allows for comparisons with common crystal lattices.⁴² A para-crystalline approach is used to obtain a crude estimate of structure and magnitude of order (Figure S15–17, Supporting Information)⁴³ however, since Bragg's law only applies to true crystals, fitting of diffuse peaks must be taken with caution.²⁹ This is particularly the case here, as the primary peak is sensitive to volume fraction, shifting to higher q with increasing volume fraction.²⁹

The 1:1.73 peak ratios indicate the formation of a weak close-packed structure,⁴² such as FCC or HCP. It should, however, be noted that the close-packed structures (fcc and hcp) are degenerate in energy and any energy difference is expected to be insignificant to nonequilibrium effects,⁴⁴ and as many of the lattice peaks are closely spaced (Table S1, Supporting Information), the HCP and FCC lattices may not be distinguished unambiguously.⁴² These 1:1.73 structure factor peaks are seen for all particle sizes at JR2KC₂ concentrations where aggregation occurs, but interestingly for the 40 nm Au NPs at 25 nM JR2KC₂ an additional peak shoulder at 1:1.25 appeared. The assemblies of 10 and 20 nm Au NPs gave a good fit to a HCP structure whereas for the 40 nm Au NPs a minimum at $q_0/q_n = 1:1.46$ was observed, suggesting a possible preference for FCC lattice rather than a HCP structure.

In the Porod region ($q^*R_g \gg 1$, where R_g is the aggregate radius of gyration), mass-fractal scattering from aggregates display logarithmic scattering.^{23,32,45,46} The Porod regions describe the aggregate mass (M), scaling with aggregate size (R_g) i.e. ($M \sim R_g^D$). Fitting this Porod region, allows for an estimate of the aggregate fractal dimension (D_f),^{23,47,48} with values between $1 < D_f < 3$ suggesting mass fractals and $3 < D_f < 4$ surface fractals. These fractal dimensions can be compared to established theories on colloidal aggregation, where the diffusion limited colloidal aggregation (DLCA) are known to display aggregates with $D_f \sim 1.8$ and reaction limited colloidal aggregation (RLCA) results in aggregates with $D_f \sim 2.1$.⁴⁹ Generally a higher D_f indicates denser aggregates with $D_f \sim 3$ indicating compact clusters. Both the shape of mass cluster distributions and their kinetics of aggregation are inherently connected to the structure of the final aggregates.^{22,47,48,50–53}

For JR2KC₂ concentrations between 0.1 to 2.5 μM , the aggregates exhibit fractal dimensions of approximately 2.8, 2.6, and 2 for 10, 20, and 40 nm Au NPs respectively (Figure 6). The 10 and 20 nm particles hence display values that are significantly higher than those predicted by the DLCA and RLCA colloidal models and approach those seen for compact clusters ($D_f = 3$).^{21,54} DLCA and RLCA are based on the idea of particle diffusivity/mobility and sticking probability with the eventual assumption that particles stick permanently. The higher the particle diffusivity/mobility, the higher the aggregate fractal dimensions. The very high fractal dimensions observed here indicates that particles do not stick permanently and are able to diffuse into denser structures, approaching a compact cluster morphology.²¹ This is consistent with fractal dimensions observed for aggregating biomolecules, which have been found to produce assemblies with significantly higher fractal dimensions than other colloidal systems. This has been explained by the reversibility of the interactions and the possibility for the constituents to rearrange with time.^{49,53,55} The fractal dimensions

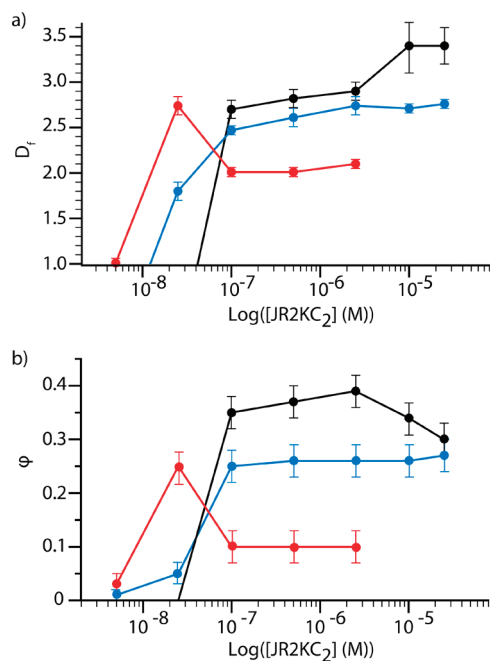


Figure 6. (a) Fractal dimensions (D_f) and (b) aggregate local volume fraction (ϕ) for JR2EC modified Au NPs with different concentrations of JR2KC₂, (red) 40 nm Au NP, (blue) 20 nm Au NP, (black) 10 nm Au NP.

observed here are also similar to those seen for assemblies of DNA coated nanoparticles.^{21,43,54}

The volume fraction and fractal dimensions decreased with increasing particle size (Figure 6), suggesting a decrease in aggregate density as the particle size increases. There was also an increase in particle correlation length (ξ) with increasing particle size and pronouncement of secondary structure factor peaks (Figure 7). The correlation length ($\xi = 2\pi/\Delta q$) was obtained by fitting the full width half-maximum (Δq) of the first structural peak in $S(q)$ ^{43,56} and provides an estimate of crystalline domain size (range of crystalline order within the aggregate).⁵⁷ The correlation lengths observed here were about $\xi = 50$ nm for 10 nm particles, $\xi = 80$ nm for 20 nm particles and $\xi = 150$ nm for 40 nm particles (Figure 7). Only minor changes in the correlation lengths were observed when increasing the concentration of JR2KC₂. These values are on the same order of magnitude as most DNA–Au NP assemblies, although significantly longer correlation lengths have been reported (up to $\xi = 500$ nm) using thermal cycling.^{20,43,58} Taking into account the size of the particles, crystalline order is seen across approximately 5 particles for 10 nm Au NPs (0.1 μ M JR2KC₂), 4 particles for 20 nm Au NPs (0.1 μ M JR2KC₂), and 3.8 particles for 40 nm Au NPs (25 nM JR2KC₂), and there is thus a slight decrease in ordering with increasing particle size. While the polydispersity of the particles also increases with size (9.4 ± 0.8 nm, 18.3 ± 2 nm, and 37.8 ± 4 nm), there is also a reduction in particle mobility (Brownian motion), which is expected to increase their sticking probability. In addition, larger particles will have wider binding regions that allow for more peptides to bridge them and restricts the extent of dynamic rearrangements. This is also confirmed for the 40 nm particles where the fractal dimensions indicate a state between DLCA and RLCA for all concentrations of JR2KC₂ causing aggregation (except at 25 nM). For the smaller particles, in addition to their higher diffusivity fewer peptides can bridge them

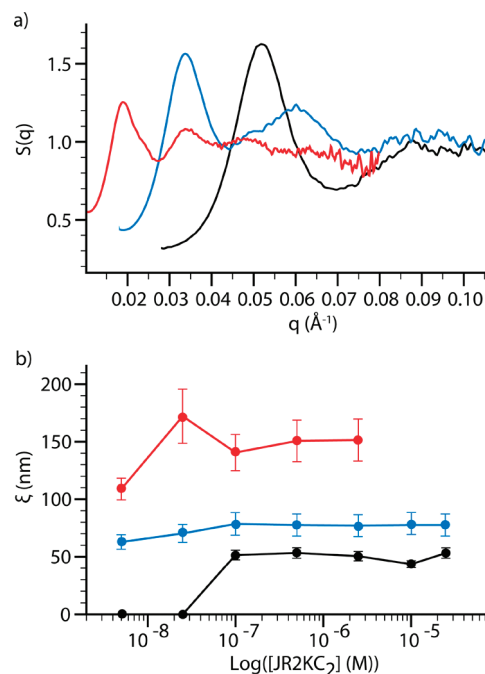


Figure 7. (a) A decrease in the full width half maxima (fwhm) of the primary peaks of the structure factor $S(q)$ and increase in pronouncement of secondary peaks was observed with increasing nanoparticle size, (black) 10, (blue) 20, and (red) 40 nm Au NPs modified with JR2EC. Data shown for 0.5 μ M JR2KC₂. (b) The correlation length (ξ) increased with increasing particle size but varied little with JR2KC₂ concentration.

because of their higher curvature, which will make them more likely to rearrange into more compact clusters with higher fractal dimensions. Considering that the polydispersity of the 40 nm Au NPs (± 4 nm) is about as the same as the size of the disulfide-linked four helix bundle (~ 5 nm), it is remarkable to see correlation lengths of up to $\xi = 150$ nm, highlighting the tolerance of soft-potentials for imperfections. For the 40 nm Au NP aggregates, we observe a small decrease in intensity at high q for the higher JR2KC₂ concentrations (Supporting Information Figure S7), indicating the possibility of minor particle precipitation.

Information obtained from both UV–vis and SAXS-data enabled us to directly correlate the optical response of the particles to the structural properties of their assemblies. A general trend of larger $\Delta\lambda_{\max}$ and $\Delta A/D$ for larger particle sizes is clearly seen, which is a result of the more efficient plasmonic coupling between the larger particles. For 10 nm particles we did not observe any aggregation at the two lowest concentrations whereas for 20 nm Au NPs, an increase in aggregate characteristics in SAXS as the JR2KC₂ concentration was increased from 5 nM to 0.1 μ M (Figure 5) was clearly seen. At a concentration of 25 nM peptide, the obtained scattering data lie in the center of this transition and the aggregate volume fraction and fractal dimensions were smaller than those seen at higher concentrations of peptide. This effect was also seen in the UV–vis spectra as a gradual increase in both $\Delta A/D$ and $\Delta\lambda_{\max}$. At 25 nM the 20 nm particles are hence starting to aggregate, forming highly branched and loosely connected networks since only a few polypeptides are associated to the particle surface and able to bridge and particle–particle charge repulsion is dominating. For

the 40 nm Au NPs, we instead observed a sharp jump in aggregate volume fraction and fractal dimension at 25 nM, indicating the formation of considerably denser aggregates. This is consistent with the large and extensive broadening of the LSPR band (Figure S4, Supporting Information) in the UV–vis spectra. A small extinction peak, however, remained at the original position indicating that a fraction of particles were still dispersed or very loosely aggregated, which explains the large deviation between $\Delta A/D$ and $\Delta \lambda_{\text{max}}$. Closer inspection of the structure factor yields the introduction of an additional broad shoulder, suggesting a broad peak at around 1:1.25, in addition to the existing HCP/FCC 1:1.73 peaks (Figure S13, Supporting Information). Soft matter systems sometimes display quasi-forbidden secondary diffraction peaks, originating from phase boundaries surrounding crystalline islands.¹³ The broad 1:1.25 peak is indicative of a macroscopically ordered material suggesting that the 40 nm particles undergo a sudden increase in ordering under these conditions. An explanation for the sharp difference in aggregate behavior for the differently sized particles at these boundary conditions can be found when considering the number of polypeptides that are associated to their surface and potentially could induce bridging aggregation. For the same concentration of JR2KC₂, the number of peptides bound to particles of different sizes varies considerably, which clearly affects the assembly process. The surface densities of peptides associated to the particles at any given concentration of JR2KC₂ were estimated from the dissociation constant of the interaction ($K_D = 0.3 \mu\text{M}$). At 25 nM there are on average about 4, 15, and 60 JR2KC₂ molecules associated to each 10, 20, and 40 nm particle, respectively. The low amount of peptides associated to the 10 nm particles is apparently not enough to cause any aggregation whereas both the 20 and 40 nm particles aggregated. The number of JR2KC₂ molecules bridging the 20 nm particles seems to be at the very limit for what is needed in order to keep the particles assembled, thus producing highly dynamic aggregates with a low volume fraction and fractal dimensions resulting in a very small shift of the plasmon band. The corresponding fractal dimension ($D_f \sim 1.8$) indicates a more branched aggregate, suggesting DLCA, which is normally indicative of a high sticking probability. However, in this case the lower fractal dimension is more likely related to the high electrostatic repulsion between the aggregated particles, which is barely balanced by the attractive forces of the bridging polypeptides. In the case of the 40 nm particles, there are enough peptides to keep the particles assembled while still allowing reversible rearrangements within the aggregates resulting in an increase in order as the peptides optimize their interactions. These structural rearrangements are also seen as a decrease in $\Delta A/D$ over time (Figure 5f) as a result of a very pronounced broadening of parts of the plasmon band (Supporting Information Figure S4) indicative of strong plasmonic coupling. At higher concentrations of JR2KC₂, the cooperative effect resulting from a larger number of peptides bridging the particles makes any rearrangements after assembly more difficult resulting in slightly less ordered assemblies with lower fractal dimensions and volume fractions. Indeed, the 20 nm particles SAXS data indicate only minor changes in aggregate morphology for concentrations of JR2KC₂ above $0.1 \mu\text{M}$, which correlates well with UV–vis data up to $25 \mu\text{M}$. At the highest peptide concentration ($25 \mu\text{M}$), the effect of particle charge reversal and saturation becomes apparent and a large fraction of the particles appears to remain dispersed causing a significant deviation between $\Delta A/D$ and $\Delta \lambda_{\text{max}}$. The lack of an optical shift

for the 10 nm Au NP at $10 \mu\text{M}$ and $25 \mu\text{M}$ JR2KC₂ indicates that the majority of particles remained dispersed although SAXS data indicate the presence of aggregates with a structure factor and a fractal dimension of 3.5. This suggests that the aggregates size has shrunk to the point where their surfaces are visible (fractal dimensions between 3 and 4 are indicative of spherical structures). It has previously been suggested that very small aggregates of Au NPs (number of particles <10) do not produce any significant shift in the LSPR band.⁵⁹ It is thus likely that some of the rapidly diffusing 10 nm particles assemble into small compact clusters before all available surface bound peptides are saturated with JR2KC₂ molecules, which then prevents further aggregation, without causing a pronounced spectral red shift. A schematic illustration of the proposed structural properties of the assemblies of the 10, 20, and 40 nm Au NPs at 25 nM and $2.5 \mu\text{M}$ JR2KC₂ is presented in Figure 8.

The separation between the assembled particles induced by the presence of the folded polypeptides can be estimated by using the hard sphere radius (r_{hs}) obtained from the sticky hard sphere model. This parameter describes the distance (from the center of the particle) at which particles repel and in this context is assumed to describe the combined particle with the immobilized polypeptides. By subtracting the radius of the bare gold nanoparticles r_{AuNP} from the hard sphere radius r_{hs} , an estimate of the size of the polypeptides can be made. This assumes that there is no preferential orientation of the particles in the aggregates based on polydispersity. In the case of the 20 and 40 nm particles, the polydispersity of the particles was about the same as the length of the peptides and as SAXS obtains rotationally and statistically averaged information, accurate values on the separation could thus not be obtained. For 10 nm Au NPs, consistent data were obtained, demonstrating a separation between the aggregated particles of $4.8 \pm 0.4 \text{ nm}$. This value is in excellent agreement with data previously obtained from electron micrographs ($4.6 \pm 0.4 \text{ nm}$) and with the expected size of the folded disulfide-linked four helix bundles ($\sim 5 \text{ nm}$),²⁴ strongly indicating that the polypeptides indeed are folded. The separation did not vary significantly for different concentrations of the bridging polypeptide in the range where aggregation was obtained.

Conclusions. This paper provides a detailed characterization of the folding-dependent assembly of polypeptide functionalized gold nanoparticles using UV–vis spectroscopy and small-angle X-ray scattering, from which we are able to extract fundamental information on the complex and dynamic interplay between a large number of factors influencing the assembly process and the resulting optical and structural properties of the aggregates. The assembly of the particles was the result of a heteroassociation and folding-induced bridging aggregation of the particles caused by the formation of a supramolecular polypeptide construct with well-defined structure. The polypeptide-modified Au NPs formed denser aggregates with a higher fractal dimension than typically seen for irreversibly aggregating colloidal systems, because of the highly dynamic and reversible nature of the molecular interactions involved in the assembly.^{46,59} The particles assembled into hcp/fcc-like structures with an interparticle separation of $4.8 \pm 0.4 \text{ nm}$, which is in excellent agreement with previously obtained TEM data and the expected size of the folded disulfide-linked four helix bundles that bridged the aggregated particles. The magnitude of structural order was similar to DNA-coated Au NPs,^{20,43,58} although not as high as reported values for systems that have been thermally cycled.⁴³ The aggregation rate,

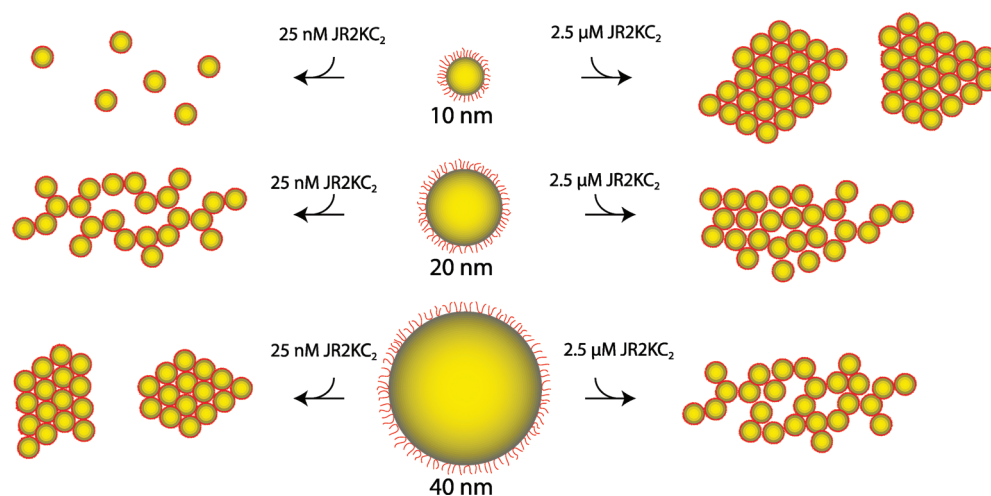


Figure 8. Schematic cross-section illustration of the proposed structures of the assemblies at $2.5 \mu\text{M}$ and 25 nM JR2KC₂ for JR2EC modified Au NPs with diameters of 10, 20, and 40 nm (JR2KC₂ omitted for clarity). At $2.5 \mu\text{M}$, aggregation was obtained for all particle sizes but large variations in ordering and fractal dimensions were observed with the 10 nm particles demonstrating the densest and most well-ordered assemblies. At 25 nM , the number of peptides associated to the 10 nm particles was not enough to induce aggregation whereas 20 nm particles formed highly branched aggregates with low fractal dimensions. In contrast, the number of peptides bridging the 40 nm particles was enough to cause extensive aggregation but still few enough to allow for dynamic reorganizations to take place, which lead to the formation of highly ordered domains.

extent of aggregation and internal ordering of the aggregates were highly dependent on the size of the nanoparticles and concentration of the bridging polypeptide. Particle diffusivity and surface curvature decrease with increasing particle size, which clearly affected the sticking probability. When polypeptide concentration was high enough to assemble the particles but still low enough to allow for structural rearrangements, densely packed and well-ordered aggregates were obtained. Smaller particles formed denser aggregates because fewer peptides were bridging them in combination with their higher diffusivity. If the particles were large enough to allow for several polypeptides to bridge them, internal reorganizations became less likely when the concentration of the bridging polypeptides was gradually increased, yielding a decrease in order and aggregate density. As the concentration of the bridging polypeptides was increased further, extensive aggregation was prevented by the saturation of the immobilized polypeptides in combination with the increase in stabilizing forces provided by the nanoparticle-associated molecules. A schematic illustration of the structural properties of the assemblies of the differently sized particles at 25 nM and $2.5 \mu\text{M}$ of the bridging polypeptide are summarized in Figure 8.

The presented data show a clear dependence of the physicochemical properties and concentration of the polypeptides and the size of the nanoparticles on the structural and optical properties of the assemblies. These are all parameters that are relatively easy to tune and the work presented here can thus act as a guide in the formulation of general principles for assembly of nanoparticles by biomolecular mediated bridging. Such guiding principles are expected to be valid for all systems that enable reversible assembly and dynamic structural rearrangements and will greatly facilitate the design of other assembly directing molecules and the development of a broad range of hybrid materials. It is also of the utmost importance to have a detailed understanding of the particle assembly mechanisms and the corresponding optical transitions for development of colorimetric biosensors. From these results, we can learn how to predict and optimize the response in colorimetric nanoparticle-based

assays in order to improve their sensitivity and robustness, which eventually will provide us with new and better tools for diagnostics and drug screening.

Materials and Methods. *Materials.* Citrate-stabilized gold colloids of approximately 10, 20, and 40 nm in diameter were purchased from British BioCell international (Cardiff, UK) and used as obtained. The polypeptides JR2KC (NAADLKKAIAK-LKKHLKAKGPCDAAQLKKQLKQAFKAFKRAG) and JR2EC (NAADLEKAIEALEKHLEAKGPCDAAQLEKQLEQAFKAFERAG) were synthesized on a Pioneer automated peptide synthesizer (Applied Biosystems) using standard fluorenylmethoxycarbonyl (Fmoc) chemistry protocols and Fmoc-Gly-poly(ethylene) glycol-polystyrene resin. The crude products were purified by reversed-phase HPLC on a semipreparative HICROM C-8 column and identified by MALDI-TOF mass spectrometry. In order to obtain JR2KC₂, lyophilized JR2KC monomers (1 mM) were dissolved in 0.1 M ammonium bicarbonate buffer pH 8, aerated for 90 min, and incubated at 4°C for at least 24 h before use. The synthesis is described in more detail elsewhere.²⁷

Analysis of the Association Constant (K_d). This analysis was performed in a custom-made spectroscopic SPR setup in Kretschmann configuration using 50 nm thick Au films thermally evaporated on glass slides with 2 nm of Cr for adhesion improvement. The collimated incident light from a fiber coupled halogen lamp at an angle of 68° provided a resonance wavelength at 700 nm, that is, within the optimal spectral region for biosensing.⁶⁰ The variations of the SPR spectral position were analyzed with a Jaz spectrometer (Ocean Optics) and a high-degree polynomial-tracking algorithm. Clean Au surfaces were incubated for at least 12 h with JR2EC ($10 \mu\text{M}$) in stagnant conditions, whereas the different concentrations of JR2KC₂ were flowed at a constant speed of $20 \mu\text{L}/\text{min}$.

Peptide Functionalization of Gold Nanoparticles. Au NPs were incubated for at least 12 h with JR2EC ($10 \mu\text{M}$) in 10 mM citrate buffer pH 6. After immobilization, nonbound peptides were removed by repeated centrifugations and the supernatant was removed and replaced with 30 mM Bis-Tris buffer pH 7.0

until the resulting concentration of peptides in solution was less than 0.1 nM. Particle concentration was estimated using UV–vis spectroscopy. The molar absorptivity (E) for the differently sized Au NPs was obtained using the method described by Xiong Liu et al.⁶¹ The particles were diluted to concentrations of 1.6 nM (10 nm), 0.4 nM (20 nm), and 91 pM (40 nm) in 10 mM Hepes, 150 mM NaCl, 0.005% (w/v) Tween20 pH 7.4, providing a constant particle surface area of $0.3 \text{ m}^2 \text{ L}^{-1}$.

Analytical Techniques. UV–vis spectroscopy was carried out on a Perkin-Elmer Lambda 25 UV–vis spectrometer at room temperature. For size determination, Au NPs were imaged and measured using a Joel 2010 TEM and ImageJ software. The size distributions were fitted with a log-normal distribution to yielding a mean sizes and standard deviations of $9.3 \pm 0.7 \text{ nm}$ ($n = 500$), $18.9 \pm 1 \text{ nm}$ ($n = 500$), and $38.4 \pm 3 \text{ nm}$ ($n = 150$). SAXS measurements were performed at the Australian synchrotron SAXS/WAXS beamline. A beam energy of 10 KeV and a low noise Pilatus 1 M detector were used; silver behenate was used as a q space calibrant.⁶² A sample detector (S-D) distance of 3 m was used for the 10 and 20 nm Au NPs and a S-D of 7 m for 40 nm Au NPs providing an accessible q range of 0.0049 to 0.2289 \AA^{-1} and 0.0023 to 0.1081 \AA^{-1} respectively. The scattering vector \vec{q} describes the difference between the wave vectors of the incident (\vec{k}_i) and diffracted (\vec{k}_d) beams, that is, $\vec{q} = \vec{k}_i - \vec{k}_d$. It has modulus $q = |\vec{q}| = (4\pi/\lambda)\sin(\theta)$ where θ is half the scattering angle and λ is the incident photon wavelength. The data was corrected for transmission, beam intensity, detector response, background scattering, and exposure time and normalized to an absolute scale. SAXS data reduction was performed using SAXS1SID in an IDL environment and with modeling and fitting carried out using Irena macros implemented in Igor Pro.^{63,64} The samples were measured inside 1 mm diameter quartz capillaries; the fluid was oscillated within the capillary, so as to reduce radiation damage to the sample. Measurements were taken dynamically across a period of 15 min, using 1 s exposure times with the first scan starting approximately 2 min after reaction initiation. Since little change with time was seen in the scattering pattern, the last data snapshot at 15 min was used for analysis.

■ ASSOCIATED CONTENT

Supporting Information. UV–vis spectra and SAXS data for all particle sizes and concentrations of polypeptides. Details on modeling and data fitting. This material is available free of charge via the Internet at <http://pubs.acs.org>.

■ AUTHOR INFORMATION

Corresponding Author

*E-mail: (M.M.S.) m.stevens@imperial.ac.uk; (M.P.R.) m.p.ryan@imperial.ac.uk

■ ACKNOWLEDGMENT

Financial support from the Knut and Alice Wallenberg Foundation (KAW) for D.A., the EPSRC and ERC Grant “NaturaLe” for M.M.S., the Swedish Research Council (VR), and the Swedish Foundation for Strategic Research (SSF) is gratefully acknowledged. B.S. acknowledges the “Ramón y Cajal” program from “Ministerio de Ciencia e Innovación” of Spain for financial support. We thank the Australian synchrotron for synchrotron time on the SAXS beamline (Grant AS093/SAXS1875) and

the extensive support of the beamline scientists (Dr. Hawley and Dr. Mudie) without whom this research could not have been performed. We thank Dr. Nicholas Schaeffer and Dr. Aaron Eberle for discussions and input.

■ REFERENCES

- (1) Shi, J. J.; Votruba, A. R.; Farokhzad, O. C.; Langer, R. *Nano Lett.* **2010**, *10*, 3223–3230.
- (2) Stupp, S. I. *Nano Lett.* **2010**, *10*, 4783–4786.
- (3) Stevens, M. M.; George, J. H. *Science* **2005**, *310*, 1135–1138.
- (4) Minelli, C.; Lowe, S. B.; Stevens, M. M. *Small* **2010**, *6*, 2336–2357.
- (5) Ghosh, P.; Han, G.; De, M.; Kim, C. K.; Rotello, V. M. *Adv. Drug Delivery Rev.* **2008**, *60*, 1307–1315.
- (6) Rosi, N. L.; Mirkin, C. A. *Chem. Rev.* **2005**, *105*, 1547–1562.
- (7) Aili, D.; Stevens, M. M. *Chem. Soc. Rev.* **2010**, *39*, 3358–3370.
- (8) Mirkin, C.; Letsinger, R.; Mucic, R.; Storhoff, J. *Nature* **1996**, *382*, 607–609.
- (9) Alivisatos, A. P.; Johnsson, K. P.; Peng, X.; Wilson, T. E.; Loweth, C. J.; Bruchez, M. P.; Schultz, P. G. *Nature* **1996**, *382*, 609–611.
- (10) Mann, S.; Shenton, W.; Li, M.; Connolly, S.; Fitzmaurice, D. *Adv. Mater.* **2000**, *12*, 147–150.
- (11) Ryadnov, M. G.; Ceyhan, B.; Niemeyer, C. M.; Woolfson, D. N. *J. Am. Chem. Soc.* **2003**, *125*, 9388–9394.
- (12) Stevens, M.; Flynn, N.; Wang, C.; Tirrell, D.; Langer, R. *Adv. Mater.* **2004**, *16*, 915–918.
- (13) Förster, S.; Timmann, A.; Schellbach, C.; Frömsdorf, A.; Kornowski, A.; Weller, H.; Roth, S.; Lindner, P. *Nat. Mater.* **2007**, *6*, 888–893.
- (14) Sepulveda, B.; Angelomé, P. C.; Lechuga, L. M.; Liz-Marzán, L. M. *Nano Today* **2009**, *4*, 244–251.
- (15) Lee, J. S.; Han, M. S.; Mirkin, C. A. *Angew. Chem., Int. Ed.* **2007**, *46*, 4093–4096.
- (16) Elghanian, R.; Storhoff, J. J.; Mucic, R. C.; Letsinger, R. L.; Mirkin, C. A. *Science* **1997**, *277*, 1078–1081.
- (17) Aili, D.; Mager, M.; Roche, D.; Stevens, M. *Nano Lett.* **2011**, *11*, 1401–1405.
- (18) Gupta, S.; Andresen, H.; Ghadiali, J.; Stevens, M. *Small* **2010**, *6*, 1509–1513.
- (19) Guarise, C.; Pasquato, L.; De Filippis, V.; Scrimin, P. *Proc. Natl. Acad. Sci. U.S.A.* **2006**, *103*, 3978–3982.
- (20) Storhoff, J.; Lazarides, A.; Mucic, R.; Mirkin, C. *J. Am. Chem. Soc.* **2000**, *122*, 4640–4650.
- (21) Park, S.; Lee, J.; Georganopoulou, D.; Mirkin, C.; Schatz, G. *J. Phys. Chem. B* **2006**, *110*, 12673–12681.
- (22) Weitz, D.; Huang, J.; Lin, M.; Sung, J. *Phys. Rev. Lett.* **1985**, *54*, 1416–1419.
- (23) Martin, J. E.; Hurd, A. *J. Appl. Crystallogr.* **1987**, *20*, 61–78.
- (24) Aili, D.; Enander, K.; Baltzer, L.; Liedberg, B. *Nano Lett.* **2008**, *8*, 2473–2478.
- (25) Aili, D.; Enander, K.; Rydberg, J.; Lundström, I.; Baltzer, L.; Liedberg, B. *J. Am. Chem. Soc.* **2006**, *128*, 2194–2195.
- (26) Aili, D.; Enander, K.; Rydberg, J.; Nesterenko, I.; Björefors, F.; Baltzer, L.; Liedberg, B. *J. Am. Chem. Soc.* **2008**, *130*, 5780–5788.
- (27) Enander, K.; Aili, D.; Baltzer, L.; Lundström, I.; Liedberg, B. *Langmuir* **2005**, *21*, 2480–2487.
- (28) Chowdhury, M.; Julian, A.; Coates, C.; Coté, G. *J. Biomed. Opt.* **2004**, *9*, 1347–1357.
- (29) Fournet, G.; Guinier, A. *Small Angle Scattering of X-rays*; John Wiley: New York, 1955.
- (30) Lindner, P.; Zemb, T. *Neutrons, X-rays, and light: scattering methods applied to soft condensed matter*; Elsevier: North-Holland, 2002.
- (31) Borsali, R.; Pecora, R. *Soft-Matter Characterization*; Springer Verlag: New York, 2008.
- (32) Beaucage, G. *J. Appl. Crystallogr.* **1996**, *29*, 134–146.
- (33) Stell, G. *J. Stat. Phys.* **1991**, *63*, 1203–1221.

- (34) Menon, S.; Manohar, C.; Rao, K. *J. Chem. Phys.* **1991**, *95*, 9186–9191.
- (35) Muratov, A.; Moussaïd, A.; Narayanan, T.; Kats, E. *J. Chem. Phys.* **2009**, *131*, 054902.
- (36) De Kruijff, C.; Rouw, P.; Briels, W.; Duits, M.; Vrij, A.; May, R. *Langmuir* **1989**, *5*, 422–428.
- (37) Vavrin, R.; Kohlbrecher, J.; Wilk, A.; Ratajczyk, M.; Lettinga, M.; Buitenhuis, J.; Meier, G. *J. Chem. Phys.* **2009**, *130*, 154903.
- (38) Robertus, C.; Philipse, W.; Joosten, J.; Levine, Y. *J. Chem. Phys.* **1989**, *90*, 4482.
- (39) Chen, S.; Rouch, J.; Sciortino, F.; Tartaglia, P. *J. Phys.: Condens. Matter* **1994**, *6*, 10855–10883.
- (40) Gazzillo, D.; Giacometti, A. *J. Chem. Phys.* **2000**, *113*, 9837.
- (41) Regnaut, C.; Ravey, J. *J. Chem. Phys.* **1989**, *91*, 1211.
- (42) Huang, Y.-Y.; Chen, H.-L.; Hashimoto, T. *Macromolecules* **2003**, *36*, 764–770.
- (43) Nykypanchuk, D.; Maye, M.; van der Lelie, D.; Gang, O. *Nature* **2008**, *451*, 549–552.
- (44) Matsen, M. *Macromolecules* **1995**, *28*, 5765–5773.
- (45) Beaucage, G. *J. Appl. Crystallogr.* **1995**, *28*, 717–728.
- (46) Norman, T.; Grant, C.; Schwartzberg, A.; Zhang, J. *Opt. Mater* **2005**, *27*, 1197–1203.
- (47) Mandelbrot, B. *The fractal geometry of nature*; W. H. Freeman and Co.: San Francisco, 1982.
- (48) Schaefer, D.; Martin, J.; Wiltzius, P.; Cannell, D. *Phys. Rev. Lett.* **1984**, *52*, 2371–2374.
- (49) Meakin, P. *Annu. Rev. Phys. Chem.* **1988**, *39*, 237–267.
- (50) Kolb, M.; Botet, R.; Jullien, R. *Phys. Rev. Lett.* **1983**, *51*, 1123–1126.
- (51) Vicsek, T.; Family, F. *Phys. Rev. Lett.* **1984**, *52*, 1669–1672.
- (52) Weitz, D.; Oliveria, M. *Phys. Rev. Lett.* **1984**, *52*, 1433–1436.
- (53) Meakin, P. *Phys. Rev. Lett.* **1983**, *51*, 1119–1122.
- (54) Park, S.; Lytton-Jean, A.; Lee, B.; Weigand, S.; Schatz, G.; Mirkin, C. *Nature* **2008**, *451*, 553–556.
- (55) Klein, R.; Meakin, P. *Nature* **1989**, *339*, 360–362.
- (56) *Applications of Synchrotron Light to Scattering and Diffraction in Materials and Life Sciences*; Ezquerro, T. A., Garcia-Gutierrez, M. C., Nogales, A., Gomez, M., Eds.; Springer Verlag: Berlin, 2009.
- (57) Macfarlane, R.; Lee, B.; Hill, H.; Senesi, A.; Seifert, S.; Mirkin, C. *Proc. Natl. Acad. Sci. U.S.A.* **2009**, *106*, 10493–10498.
- (58) Park, S.; Lazarides, A.; Storhoff, J.; Pesce, L.; Mirkin, C. *J. Phys. Chem. B* **2004**, *108*, 12375–12380.
- (59) Kim, T.; Lee, C.; Joo, S.; Lee, K. *J. Colloid Interface Sci.* **2008**, *318*, 238–243.
- (60) Otte, M. A.; Sepúlveda, B.; Ni, W.; Perez-Juste, J.; Liz-Marzan, L. M.; Lechuga, L. M. *ACS Nano* **2009**, *4*, 349–357.
- (61) Jain, P.; Lee, K.; El-Sayed, I.; El-Sayed, M. *J. Phys. Chem. B* **2006**, *110*, 7238–7248.
- (62) Huang, T.; Toraya, H.; Blanton, T.; Wu, Y. *J. Appl. Crystallogr.* **1993**, *26*, 180–184.
- (63) Kline, S. R. *J. Appl. Crystallogr.* **2006**, *39*, 895–900.
- (64) Ilavsky, J.; Jemian, P. *J. Appl. Crystallogr.* **2009**, *42*, 347–353.